LoLX Co-op Term Documentation and Report

Pierce Comerford

September 13, 2024

1 Overview

This report largely focuses on the work done between early May and late August on the liquid xenon purity monitor for LoLX, with some supplementary documentation on the data acquisition system (DAQ) for pion lifetime measurement.

1.1 The Purity Monitor

Impurities in liquid xenon will affect light yield in LXe-based scintillators, such as those used for nEXO and PIONEER. To ensure the effective light yield is always well-known, a purity monitor is needed to keep track of liquid xenon purity for the LoLX project. The purity monitor generates electrons at a photocathode and measures the signal both here and at the anode to find the average lifetime of an electron in the liquid xenon, which can be related back to purity.

Here, the photocathode is a think layer of gold on a MgF_2 window. Electrons are emitted when gold is stimulated with light with higher energy than its workfunction, according to the photoelectric effect. Gold's workfunction is approximately 5.10 – 5.47 eV(11), so light with $\lambda \lesssim 230$ nm should be useful for kicking out electrons. The photocathode is stimulated by a 20 W Hamamatsu L12745-01-3 flash lamp, with light output between 160 nm and 7500 nm.

The number of electrons yielded for a given light pulse depends on the quantum efficiency of the photocathode. This peaks at a thickness of approximately 10 nm, where QE is between 0.2 and 0.4(2).

The purity monitor follows a double-gridded drift chamber design, similar to those used by multiple groups for nEXO(7-10). The purity monitor will need to work in the LoLX cryostat at McGill (see the LoLX Twiki page), and is thus subject to spatial constraints, namely that the drift length is only approximately 3.88 cm. The measured variable is the drift time T of the electron (which differs between the regions marked 1, 2 and 3, in Fig. 1), which can be approximately related to the electron lifetime τ_e by(4)

$$\tau_e \approx \frac{-t_2}{\ln\left(Q_\mathrm{a}/Q_\mathrm{pc}\right) + \ln\left(t_1/t_3\right)}, \tag{1}$$

where Q_pc and Q_a are the charge at the photcathode and anode (the measurable quantities), respectively, and t_r is the drift time in region r (see Fig. 2).

Finally, we get a measure of the purity of the drift medium (in this case, liquid xenon) by(3)(5)

$$\tau_e = \frac{1}{\sum_i k_i C_i} = \frac{1}{k^\mathrm{eff}_{\mathrm{O}_2} C^\mathrm{eff}_{\mathrm{O}_2}}, \tag{2}$$

where k is the electron attachment rate of the species, C is its concentration, and 'eff' specifies that the third term is in terms of a standard effective measure of O_2-equivalent, since differentiation between species would be unfeasible.

The drift velocity of electrons in liquid xenon at an electric field strength of 1600 V/cm is $\approx 1.81964284 \times 10^{-1}$ cm/μs, according to the NEST software package, and the drift length of the purity monitor is 3.88 cm, corresponding to a drift time of $\approx 21.32\,\mu s$.

Taking $k \approx 4 \times 10^{10}(6)(1)$, equation (1) tells us that we have a sensitivity on the order of about 10^{-6} mol, or, since O_2 has a molar mass of approximately 30 g/mol, on the order of 10 ppb, which is very much acceptable.

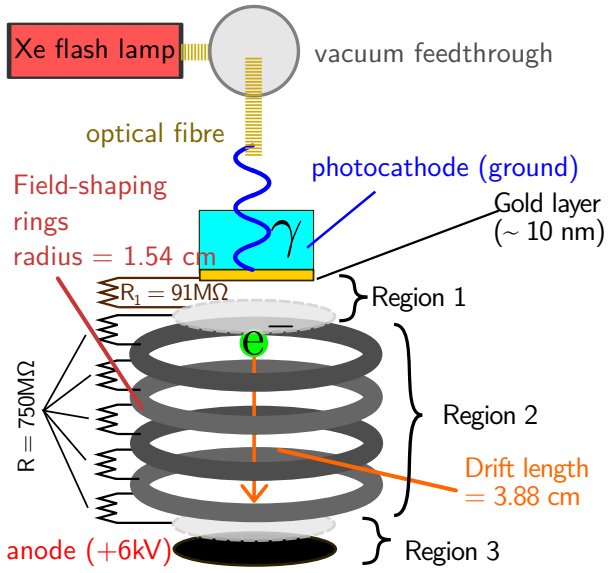

Figure 1: Schematic diagram of the purity monitor, with optoelectrical components highlighted. Region 1 is between the photocathode and the first grid, Region 2 is between the two grids, and Region 3 is between the second grid and the photocathode.

Field-shaping rings are used to keep the electric field uniform, which among other things simplifies calculations simplifies calculations and allows efficient electron transport. The uniformity of the electric field is examined in detail in the Simulations section.

1.2 Table of resistance values

Resistor	Resistance
R_1 (between cathode and first grid)	91 MΩ
R_2 (all other resistors)	750 MΩ

1.3 Table of electric fields

Region	Field Norm (ideal)
1	800 V/cm
2	1600 V/cm
3	3200 V/cm

2 Testing of Components

For more details, data, and code used in analysis and testing, see this Github repository.

To optimize the sensitivity of the apparatus as outlined in the previous section, it is necessary to test the relevant properties of the components of the apparatus. In particular, the properties of various components between the flash-lamp and the photocathode were looked at in detail.

To see how much light is lost between light source and photocathode, and to test for wavelength dependence of components, the power output of seven monochromatic LEDs was measured using a ThorLabs S120VC photodiode power sensor (after calibration) connected to a ThorLabs PM101 power meter in 5 configurations, listed below. Note that the Fibre 1 is a fibre of radius 1 mm and length 0.4826 m, and the Fibre 2 is of radius 0.6 mm and length 0.7366 m. The LEDs are housed in a casing with a built-in SMA connector for use with the optical cables, and the S120VC was fitted with an SMA fixture. The 'SMA-SMA adaptor' is just a male-male connector.

2.1 Configuration key

- Configuration A (*dropped, see below*): LED → SMA-SMA adaptor → S120VC → PM101
- Configuration B: LED → Fibre A → S120VC → PM101
- Configuration C: LED → Fibre B → S120VC → PM101
- Configuration D: LED → Fibre A → SMA-SMA adaptor → Fibre B → S120VC → PM101
- Configuration E: LED → Fibre A → SMA-SMA adaptor → vacuum feedthrough → SMA-SMA adaptor → Fibre B → S120VC Fibre B

The LEDs ranged from 255 nm (UV) to 630 nm (red). No appreciable wavelength dependence was found above 255 nm, however it is shown later that an important dependence is found below 193 nm. It was found to be impossible to get reproducible results using configuration A, since the geometry of the LED casing made the power sensor highly sensitive to the tightness of the SMA-SMA adapter on the fitting. Configuration B was used instead of Configuration A as a means of comparing relative light yield.

2.2 Table of LED Specifications

Label	Color	Wavelength (nm)
R	Red	620
Y	Yellow	590
G	Green	520
B	Blue	460
V	Violet	365
UV1	Not visible	310
UV2	Not visible	255

At room temperature, the FHWM of the distribution of each LED is approximately 10 nm.

The light yield L in configuration C for each LED dropped only to the extent enforced by the geometrical properties of the fibre, that is,

$$\frac{L_C}{L_B} = \frac{\text{Area}_C}{\text{Area}_B} = \frac{\text{Radius}_C^2}{\text{Radius}_B^2} \approx 36\%. \tag{3}$$

The relative drop in light yield from configuration D to E is also promising: the addition of the vacuum feedthrough does not affect light yield much (see Fig. 2).

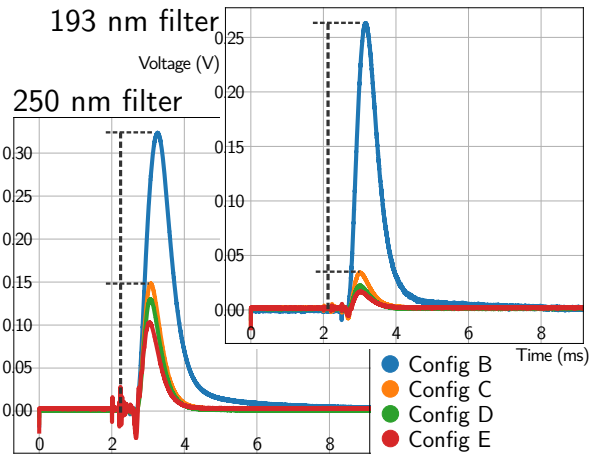

Figure 2: Comparison of pulses from configurations B, C, D, and E through 250 nm and 193 nm light filters. Compare especially pulse-areas of C to B to note wavelength-(in)dependence, and E to D to light loss due to vacuum feedthrough. More detailed versions of these plots can be generated using the `signal` program in the Github repository. (Both plots on same scale).

2.3 Photocathodes

Following Claire Hamilton's work(2) in the previous term, six photocathodes arrived in May from SFU, with an adhesive layer to allow the gold to stick to the substrate, which in this case is a 1mm thick MgF_2 window. Characterising these mainly involved testing their charge yield when provided light from the Hamamatsu L12745-01-3 20W xenon

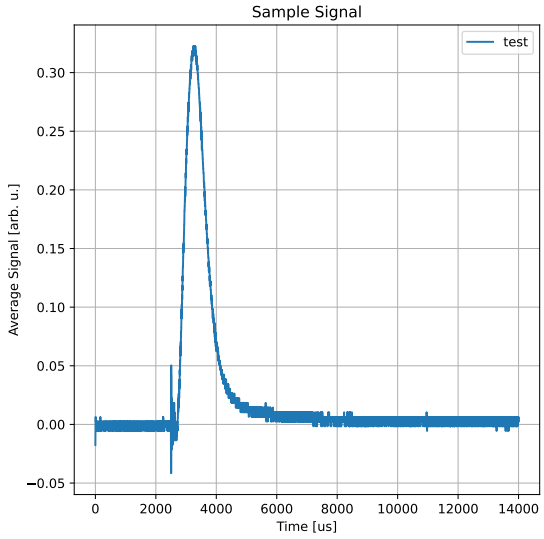

Figure 3: Sample plot of a pulse as taken from the oscilloscope.

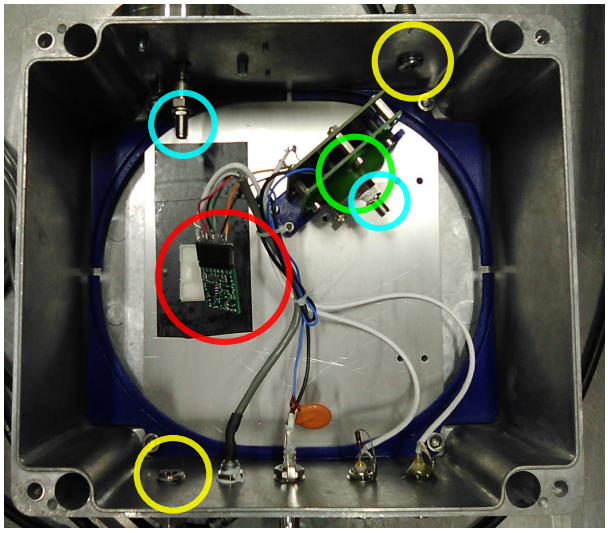

Figure 4: The box in which photocathodes were tested, with photocathode holder, gas inlet/outlet (interchangeable), SMA connector, and amplifier highlighted.

flashlamp, in terms of the pulse-area of the signal collected at the cathode.

There are three thicknesses of photocathode, and two of each thickness: 10 nm, 20 nm, and 30 nm. Twins are differentiated by having either a blue or red marker on the rim.[1]

Photocathodes were carefully placed in the green 3D-printed photocathode holder in the test box (Fig. 3). When the box is sealed, argon is passed into the outlet at a flow rate of 150 mm and exhausted through the window of the lab. A labview program automatically triggers the flash lamp and then waits at 10 minute intervals, since too small an interval would create more data than there is space available. The pulses are digitized by a Siglent SDS1204X-E oscilloscope at a sample rate of approx. 1 GSa/s, and sent back to the labview program via USB, where they are saved as `txt` files. For each text file, the pulse area is found and the pedestal is subtracted, and the charge yield thus is given as the pulse area times a conversion factor of 0.56 to take into account amplifier gain. The charge yield as a function of time is given in Fig. 4.

As expected, the 10 nm photocathodes provide the highest charge yield, but give less reproducible results, due to the relatively high manufacturing error (the gold layer is only a few atoms thick). Nevertheless, they allow charge in

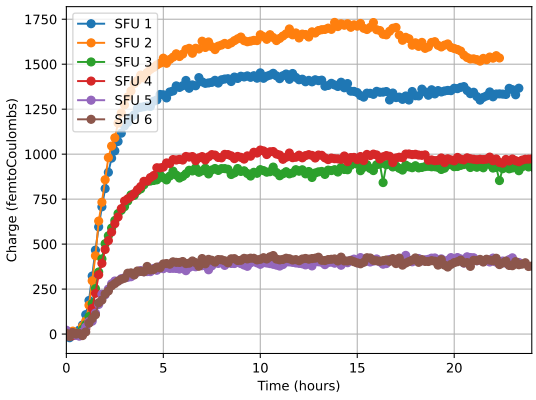

Figure 5: Charge yield of all 6 SFU photocathodes as a function of time. Note that at the beginning, the box is still flushing out air impurities and getting rid of residual air on the inner surface. After some amount of time, this plateaus.

[1] In the analysis files in the above-mentioned github link, and in Fig. 3, the following key is used:

- SFU 1 = 10 nm, blue
- SFU 2 = 10 nm, red
- SFU 3 = 20 nm, blue
- SFU 4 = 20 nm, red
- SFU 5 = 30 nm, blue
- SFU 6 = 30 nm, red.

the range of a few picoCoulombs to be collected, which is above the hundreds of femtoCoulombs initially expected.

2.4 Optical filters

Two Edmund Optics band-pass filters, one 193 ± 7.5 nm and the other 250 ± 5 nm, were also examined. They were placed in a 3D-printed fixture which was fitted directly over the sensor on the S120VC. Sample pulses were collected and averaged from these for all four of the above-mentioned configurations. It was found that configuration C gave considerably lower light yield than B for the 193 nm filter, and thus that Fibre B does have a strong wavelength dependence below approximately the 200 nm point. For this reason, it will be replaced in the final design with a 1 mm fibre identical to the one in configuration B. Fig. 2 shows the discrepancy in greater detail.

3 Simulations

For more details and simulation code, see this Github repository. Note that some of the files are too big to store on Github, and can be found instead on `vkdecay`.

Claire(2) initially designed a simplified model of the purity monitor from within COMSOL, with a variable number of perfectly circular field-shaping rings, embedded in a cylinder which mimics the environment within the LoLX cryostat. After the final CAD model of the purity monitor was developed by Nicolas (Fig. 5), it was imported into Claire's model and assigned material properties. These do not necessarily reflect the materials used in the final assembly, but should have close enough properties. In particular, the old model of the grid (which is a rigid 30×30 mesh of wires, enclosed in a circle of radius 5 mm) is retained from the old model, as is the cylinder of liquid xenon which mimics the cryostat. Importantly, insulating and conducting elements have been properly defined (in general as either a generic ABS plastic or a metal).

3.1 Table of materials assigned to model components

Component	Material	Relevant Properties
Photocathode	Gold	Accuracy
Anode	Copper	Good conductor
Walls, PCBs, etc	ABS Plastic	Insulator
Grid mesh	Kanthal cuprothal	Inherited from old model
Drift Medium	Liquid Xenon	Garfield++ Compatibility
Shaping rings	Stainless Steel	Conductor
Rivets, SMA, etc	Stainless Steel	Conductor

The electric field was calculated from within this model, shown in Fig. 7. This, along with the model itself, were imported into a Garfield++ program to simulate drift paths through the purity monitor. Since Garfield++ is only designed to deal with gases, the NEST software package was used to generate a `.gas` file specifying a pseudo-gas with the same electron transport properties as liquid xenon – specifically, drift velocity and diffusion information. A Singularity container with ROOT, Garfield++, and NEST preinstalled and pre-configured, which may aide in bootstrapping the simulation code, is located here.

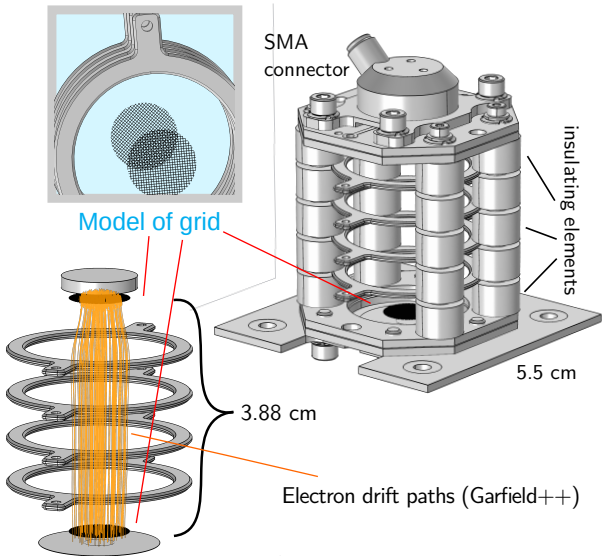

Figure 6: Purity monitor CAD model, as seen in COMSOL.

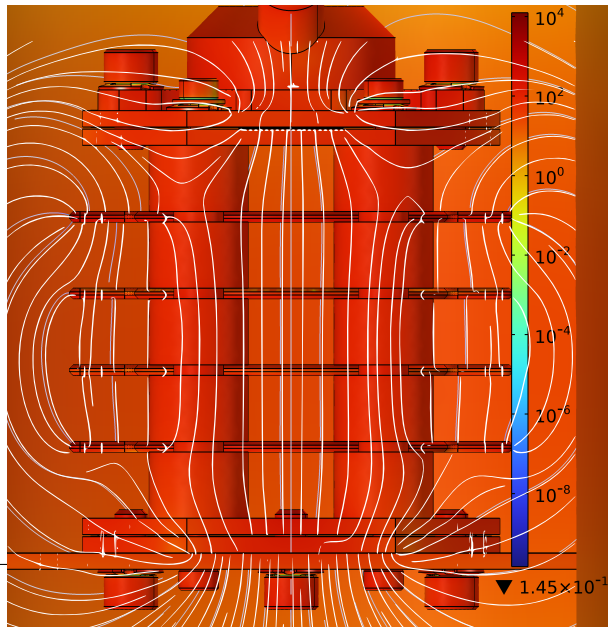

Figure 7: Electric field lines inside of purity monitor, generated in COMSOL.

4 The DAQ

Some work was also done on setting up the data acquisition (DAQ) system for the pion lifetime measurement, mostly following the guide laid out by Jack Charlton. Currently, a MIDAS server is installed on my account on `vkdecay`, configured for two separate crates. As it stands,

the second crate is not activated, as it is yet to be obtained and installed. The single crate is laid out as shown in Fig. 8. Instructions for enabling it, as well as reproducing the steps to installing the requisite software (specifically for `vkdecay`; supplementary to the guide, which is more generic), are outlined on the eLog (see those flagged in the DAQ category).

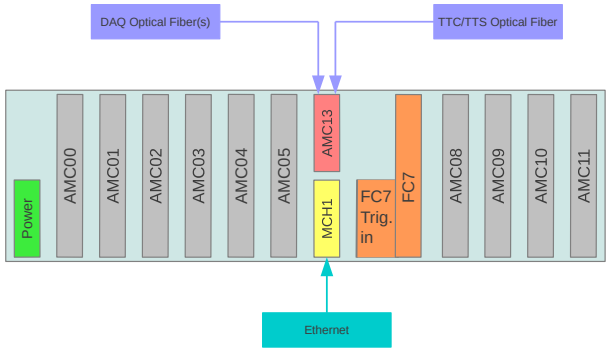

Figure 8: Schematic layout of current DAQ crate, in the Development Laboratory, adapted from the guide.

The FC7 board (for TTC of the AMCs) is not currently installed, since in late July it was noticed that damage was done to the board which renders it potentially inoperable (Fig. 8). Alex Sorokin is currently working on re-soldering the damaged components.

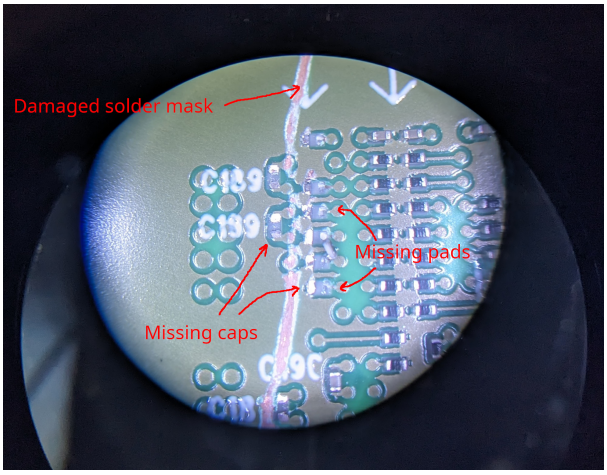

Figure 9: Damage done to the CERN FC7 board in the DAQ, courtesy of Bob Velghe.

There are three methods of communicating with the DAQ. An optical SPF+ link connects directly to the AMC13 for data acquisition, while a serial link (the SER port on the MCH) is used for low-level configuration of the MCH. Regular interface with the MCH should be done using the GBE1 connection, using the IP address 192.168.100.15. A secondary network card (labelled 'to MCH') has been installed for this purpose.

5 Next Steps

Final assembly of the purity monitor has taken place. Currently it is in the test box, replacing the old setup of a photocathode stand as pictured in Fig. 3. Tests done by Leonid show very little signal below 600 V, and an as-yet unidentified noise signal, both of which are likely due to the relatively low purity of the test box's argon.

Much of the software setup for the DAQ has been done. It is still necessary to assign an IP address to the AMC13 by interfacing with it from the MCH through the backplane of the crate, so that communication can be done through the optical link. Currently, this involves establishing a connection with the MCH over the GbE1 link, which is assigned the interface name `enp7s0`. However, attempting to ping or ssh into the MCH's IP address using this link has been so far unsuccessful. It is possible that this could be to do with low-level MCH configuration, which can be changed using the serial link, although the USB serial link is unoperational on `vkdecay`, despite working on other Linux-based computers. This might be due to Alma Linux having a different USB kernel module setup than is standard, but this remains to be explored.

[1] A. Ferella and F Arneodo and N. Canci and A. Corsi and B. Romualdi and A. Rotilio and E. Tatananni, *Purity measurements in Liquid Xenon. Electron lifetime dependence on circulation time and rate.*, Laboratori Nazionali del Gran Sasso, 2006.

[2] Claire Hamilton, *Purity Monitor Final Report*, 2024.

[3] E. Aprile and R. Mukherjee and M. Suzuki, *Measurements of the lifetime of conduction electrons in liquid xenon*, Nuclear Instruments and Methods in Physics Research, 1990.

[4] Elena Aprile and Aleksey E. Bolotnikov and Alexander I. Bolozdynya and Tadayoshi Doke, *Noble Gas Detectors*, Wiley-VCH, 2006.

[5] G. Plante and E. Aprile and J. Howlett and Y. Zhang, *Liquid-phase purification for multi-tonne xenon detectors*, Eur. Phys. J., 2022.

[6] George Bakale, *Effect of an Electric Field on Electron Attachment to SF6, N2O, and O2 In Liquid Argon and Xenon*, J. Phys. Chem, 1976.

[7] Haiwen Xu and Zepend Li, *Xenon Purity Monitor at UCSD*, 2024.

[8] Kolo Wamba and Peter Rowson, *Characterization and Upgrades for the SLAC XPM System*, 2024.

[9] Marie Vidal, *Construction of a Purity Monitor @Stanford*, 2024.

[10] Sierra Wilde, *Status of Electronegative Impurity Measurements at Yale*, 2024.

[11] William Haynes, *CRC Handbook of Chemistry and Physics*, CRC Press, 2016.